



University of
Massachusetts
Amherst

Role of GO and r-GO in resistance switching behavior of bilayer TiO₂ based RRAM

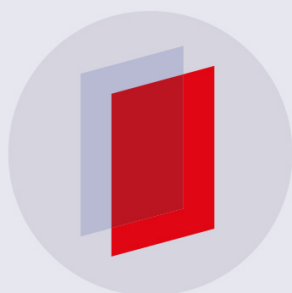
Item Type	article;article
Authors	Srivastava, Siddharth;Dey, Pritam;Asapu, Shiva;Maiti, Tanmoy
DOI	http://dx.doi.org/10.1088/1361-6528/aae135
Rights	UMass Amherst Open Access Policy
Download date	2024-12-02 10:54:04
Link to Item	https://hdl.handle.net/20.500.14394/20870

PAPER

Role of GO and r-GO in resistance switching behavior of bilayer TiO₂ based RRAM

To cite this article: Siddharth Srivastava *et al* 2018 *Nanotechnology* **29** 505702

View the [article online](#) for updates and enhancements.



IOP | ebooks™

Bringing you innovative digital publishing with leading voices to create your essential collection of books in STEM research.

Start exploring the collection - download the first chapter of every title for free.

Role of GO and r-GO in resistance switching behavior of bilayer TiO₂ based RRAM

Siddharth Srivastava¹, Pritam Dey¹, Shiva Asapu^{1,2} and Tanmoy Maiti¹ 

¹ Plasmonics and Perovskites Laboratory, Department of Materials Science and Engineering, Indian Institute of Technology Kanpur, Kanpur, UP 208016, India

² Department of Electrical and Computer Engineering, University of Massachusetts Amherst, MA 01003, United States of America

E-mail: tmaiti@iitk.ac.in

Received 2 July 2018, revised 4 September 2018

Accepted for publication 13 September 2018

Published 9 October 2018



CrossMark

Abstract

Graphene-based resistance random access memory devices (RRAMs) have shown promise as a suitable replacement for flash memories, owing to their fast switching speed, low programming voltage, better scalability and great reliability. Furthermore, recent research works have shown bi-layer RRAM devices exhibiting better performance along the same parameters, where titania is one of the most commonly used materials. In the present work, we have studied the resistance switching behavior in a bi-layer RRAM device structure of TiO₂ with graphene oxide (GO) and reduced graphene oxide (rGO). Switching mechanism in these devices has been investigated by detailed experimental characterization in conjunction with a finite element modeling (FEM) simulation. A dual conical conductive filament has been used in the present work, based on the modeling of the electroforming process carried out by FEM. It has been demonstrated that for the GO/TiO₂ based hybrid RRAM device structure, GO acts as an active filament formation layer, whereas in the rGO/TiO₂ bi-layer structure, rGO acts as a mere electrode.

Keywords: RRAM, bi-layer oxides, graphene

(Some figures may appear in colour only in the online journal)

Introduction

Non-volatile memories (NVMs) are essential to the electronics industry. The most widely used NVM, flash memory, is reaching a physical limit, which has motivated the search for alternative memory devices. Resistance random access memory (RRAM) devices have come up as one of the most suitable replacements in recent years. Compared to flash memories, they have extremely fast switching speeds, lower programming voltage, better scalability, and great reliability [1].

A wide range of materials such as transition metal oxides (e.g. HfO₂ [2], TiO₂ [3], Al₂O₃ [4], Ta₂O₅ [5], ZnO [6], VO₂ [7], etc.), perovskite oxides (e.g. SrTiO₃ [8], YMnO₃ [9], etc.) and chalcogenides (e.g. Ag/Ge_{0.25}Se_{0.75}, Ge₂Sb₃Te₅ [10], etc.) have been found to show resistive switching. A typical device structure of an RRAM contains a switching layer sandwiched between top and bottom electrodes. Recent research works have shown that devices with bilayer oxide

configuration exhibit enhanced switching speed [11], endurance [12], retention [13], and lower switching voltage [14], as compared to single layer devices.

A variety of carbon-based materials, like oxygenated amorphous carbons [15], amorphous carbons [16] and graphene oxide (GO) [17], too, have shown resistive switching behavior in recent times. Among many attractive features of these RRAMs, forming-free behavior, flexibility, and multi-level-switching make carbon-based RRAMs desirable [18]. Recently, a comprehensive study [18] on graphene based RRAMs has predicted that although GO and reduced graphene oxide (rGO) have shown some promise, they should be combined with other materials in bi-layer RRAM to further improve their performances [18–21]. One of the most important aspects of carbon-based RRAMs is their high temperature retention (~250 °C) [22], which makes them attractive for application in harsh environments. Table 1 summarizes the performances of carbon-based (GO, rGO and graphene) RRAMs in comparison with other RRAMs, based

Table 1. Comparison of carbon-based RRAMs with TMO based RRAMs.

	Device structure	SET/ RESET (V)	Power cons.	DC reset current (A)	Switching time	Endurance (cycles)	Data retention	$\frac{I_{ON}}{I_{OFF}}$	References
CARBON-BASED RRAMs	ITO/GO/Ag	-0.6 (SET)	—	$\sim 2 \times 10^{-3}$	—	—	$>10^3$ s	10^4	[25]
	PEN/Ti/Pt/GO/Ti/Pt	3.5/-3.5	—	$\sim 10^{-4}$	<10 ns	$>10^3$	—	10^2	[26]
	Al/GO/ITO	-1.6/2	—	$\sim 10^{-2}$	—	>100	10^7 s	10^3	[27]
	Ag/ZrO ₂ /SLG/Pt	1/-1	$\sim 10^4$ W	$\sim 10^{-2}$	<30 ns	$\sim 10^6$	10^4 s	10^9	[28]
	Al/PFCF/rGO/ITO	-1/2.5	—	$\sim 10^{-2}$	—	10^8	10^4 s	10^4	[29]
	Pt/Ti/GO/Pt/Ti	-3.5/3.5	$\sim 10^4$ W	8×10^{-5}	<5 ns	$>10^4$	$>10^5$ s	10^3	[19]
	G/TiO _x /Al ₂ O ₃ /TiO ₂ /G	+2.5/-1	~ 100 pW	$\sim 10^{-11}$	—	200	10^4 s	10^4	[30]
	TiN/HfO _x /G/Pt	-0.2/0.2	~ 1 μ W	$\sim 10^{-6}$	—	>1600	10^5 s	~ 100	[31]
	Pt/GO/PCMO/Pt	-1/0.5	—	2×10^{-3}	—	>150	10^4 s	~ 100	[21]
Al/Au/P3HT/Al/ZnO-G QDs/Al/SiO ₂ /Si	-5/5	—	$\sim 10^{-3}$	—	100	10^4 s	10^3	[20]	
TMO-BASED RRAMs	Pt/HfO ₂ /Ta	+0.5/-1	—	10^{-3}	<5 ns	1.2×10^{11}	>10 yrs	20	[32]
	Pt/TaO _{2-x} /Ta ₂ O _{5-x} /Pt	-1/+2	—	3×10^{-5}	<10 ns	10^{11}	>10 yrs	20	[11]
	TiN/HfO _x /Hf/TiN	+0.5/-0.5	10-20 μ W	—	5 ns	5×10^7	10 yrs	>50	[33]
	Ta/aSi/Al ₂ O ₃ /Cu	+3.6/-2	—	10^{-9} (SET)	<10 ms	5×10^2	10^4 s	>100	[34]
	Pt/TaO _x /Pt	-0.9/+2	—	170	10 ns	10^9	>10 yrs	10	[35]
	Pd/Gd ₂ O ₃ /Pt	+1/+0.7	—	0.035	—	60	>10 yrs	$>10^6$	[36]

*(PEN = polyethylene naphthalate) (SLG = single layer graphene) (PFCF = polymeric fluorocarbon) (P3HT = polythiophene) (QD = quantum dot) (PCMO = Pr_{0.7}Ca_{0.3}MnO₃).

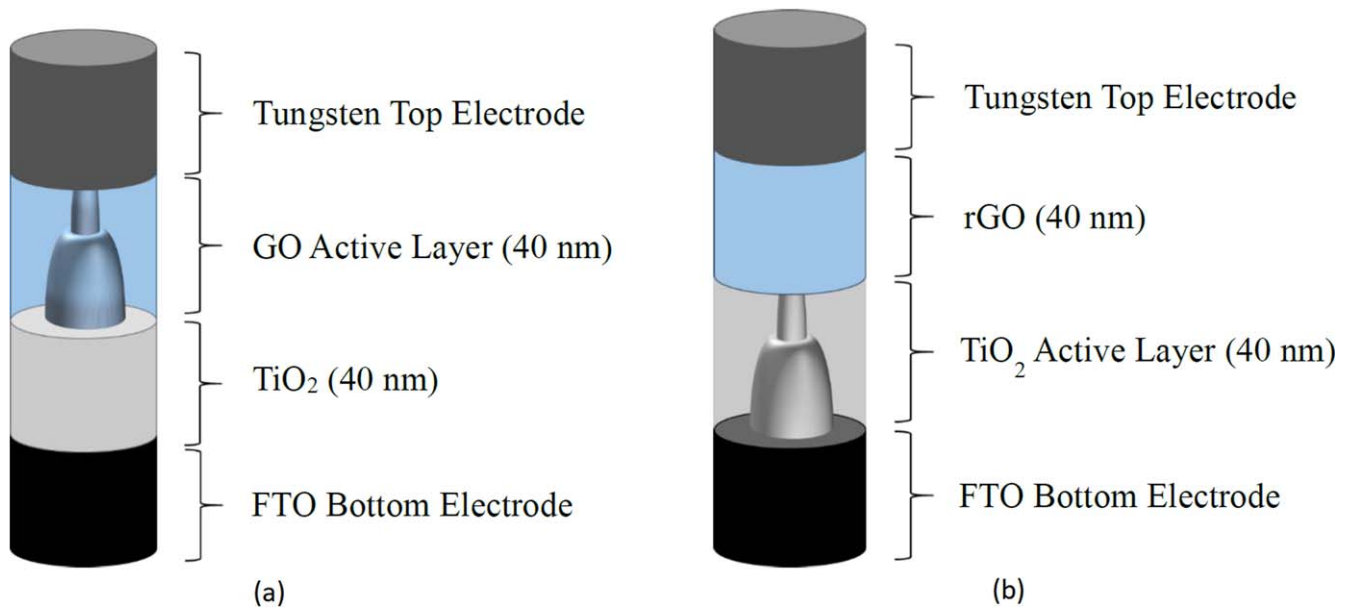


Figure 1. Device configurations modeled using dual-conical filaments in active layers.

on Si and transition metal oxides (TMO), reported in the literature. Although research on GO and rGO based RRAM devices have been initiated very recently, there has been significant progress in terms of device performance. However, there is much more scope for improvement in factors such as data retention, endurance etc. More importantly, the resistive switching mechanism in these carbon-based RRAMs has been poorly understood. GO heterostructure with polyvinylidene difluoride (PVDF) electrodes—PVDF/GO/PVDF [23] has been considered, where the observed bipolar switching has been attributed to the formation and breakage of oxygen vacancy conduction filament. A composite GO-based RRAM has also been reported with TiO₂ nanoparticles [24], where the switching has been attributed to electron trapping and de-trapping in the composite film. Recently, Pt/GO/Ti/Pt-based RRAM device structures have shown excellent endurance and retention performance, along with faster switching (sub 5 ns) speed [19]. They have attributed the resistive switching mechanism to redox reactions in the Ti/GO interface, resulting in the formation of TiO_x in the interface layer.

However, bilayer configuration consisting of TiO₂ and GO or rGO has never been reported in literature. Although, TiO₂ has been investigated extensively as a single layer structure. Moreover the advantage of better scalability and switching speed have been reported, when TiO₂ has been used in a bi-layer RRAM device structure with TaO_x [37], SiO_x [38], Al₂O₃ [39], HfO₂ [40] etc. Hence, we have chosen TiO₂ in the present work to investigate the switching mechanism of bi-layer RRAM. Although GO or rGO based memories have been investigated in the recent past [18], the switching mechanism of GO reported in literature is somewhat conflicting and confusing. Moreover, several questions

remain unanswered as of today: (a) what is the specific role of GO/rGO in the resistive switching process? (b) Does the switching take place due to bulk mechanisms in the switching layer, or properties of interface with electrode or buffer layer? (c) Are they playing the role of electrode, filament formation layer or oxygen vacancy reservoir?

In the present work, an attempt has been made to answer these questions, regarding the specific role of GO and rGO in the bilayer device configuration with TiO₂. Two separate device structures have been fabricated: W/GO/TiO₂/FTO and W/rGO/TiO₂/FTO, where fluorine-doped tin oxide (FTO) acts as the bottom electrode deposited on glass substrate. Furthermore, to understand the switching mechanism in these bilayer RRAM device structures, a finite element modeling (FEM) simulation has been carried out using COMSOL Multiphysics software. Since the migration of oxygen vacancies plays a dominant role in the switching behavior of GO-based RRAMs [18, 25], the filamentary model [3, 5, 23, 41, 42] has been widely used to understand the underlying switching mechanism. Furthermore, an electroforming process has been simulated using FEM. To the best of our knowledge this is the first report on the temporal profile of the electroforming process demonstrated by COMSOL FEM.

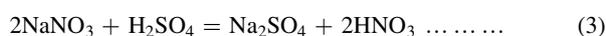
Based on the simulation results of electroforming, a dual conical conductive filament model has been utilized for the switching mechanism, as demonstrated in figure 1. In this report, we have shown that simulation corroborates with experimental data when GO acts as the filament formation layer in the W/GO/TiO₂/FTO device structure, where TiO₂ acts as the reservoir of oxygen vacancies. On the other hand, rGO acts as an electrode in the W/rGO/TiO₂/FTO structure, where TiO₂ acts as the filament formation layer.

Experimental

Materials

Graphite powder (100 mesh, 99.9995%), hydrogen peroxide (H₂O₂, 30%), sodium nitrate (NaNO₃, 99.0%), potassium permanganate (KMnO₄, 99.0%), sulfuric acid (98%), hydrazine hydrate (50%–60%), ammonium hydroxide solution (NH₄OH, 25% in H₂O), Whatman 41 filter paper, titanium isopropoxide (Ti[OCH(CH₃)₂]₄, TTIP 97%), absolute ethanol, hydrochloric acid (37%) and FTO coated glasses (~13 Ω, TEC15) have been purchased. All the reagents have been used without any further purification.

Synthesis



To prepare graphite oxide, a modified Hummer's technique [43] has been employed. Graphite powder (1 gm) and NaNO₃ (0.5 gm) have been mixed in 2:1 ratio on an ice-water bath. 23 ml sulfuric acid has been added drop-wise with simultaneous stirring, followed by 3 gm KMnO₄. After 20 min, the ice-water has been removed. The slurry has been diluted with warm deionized (DI) water, followed by heating at 90 °C for 30 min. 30% H₂O₂ has been added dropwise to the slurry until the bubbling disappeared, resulting yellow solution. The filtrate has been centrifuged to make the pH neutral. Then, the thick slurry has been lyophilized to get graphite oxide flakes.

Graphite oxide slurry (10 mg in 100 ml H₂O) has been sonicated for 2–3 h. 315 μL 25% NH₄OH has been added, followed by 35 μL hydrazine hydrate. After 10 min in the ambient atmosphere, it has been refluxed for 4 h. at 90 °C and centrifuged at 7000 rpm for 20 min before drying.

A titania compact layer has been fabricated from titania sol prepared by mixing 175 μL TTIP dropwise to 1.25 ml ethanol. Separately, 17.5 μL 2N aq. HCl solution has been mixed with 1.25 ml ethanol. The TTIP-ethanol solution has been added to the HCl-ethanol solution drop-wise with simultaneous stirring. Before the deposition, the solution has been sonicated followed by filtration (PVDF syringe filter) [44].

Device fabrication

All the studied thin film samples have been fabricated on FTO coated glass substrates (20 mm × 20 mm). The glass substrates are washed by sonication with soap (Hellmanex III) in warm DI water (v/v = 2:100) followed by isopropanol and acetone/water mixture (v/v = 1:1). Before the deposition, substrates have been treated in a UV–O₃ chamber for 10 min [45].

A spin coating technique has been used to obtain all the thin film samples. 60 μL titania sol has been dispensed on

FTO coated glass substrate, rotating at 4500 rpm for 30 s. Then, the annealing of TiO₂ film has been carried out at 500 °C for 4 h. A 2.5 °C min⁻¹ heating rate has been followed with 10 min holding at 125 °C, 200 °C, 300 °C, and 400 °C. GO (10 mg/100 ml, aq) and graphene (10 mg/100 ml, aq) have been spin coated at 4000 rpm for 30 s, followed by annealing at 80 °C for 10 min.

Characterization

The thickness of the as-fabricated thin films has been measured using an optical profilometer (Bruker GT-KO). The thin film samples have been characterized by x-ray diffraction (XRD) and Raman spectroscopy techniques using a PANalytical x-ray diffractometer X'PERT PRO and Action Spectra Pro SP-2500, respectively. A 532 nm laser of 50 mW power with 10% intensity has been used for recording the Raman spectra in the range of 700–3500 cm⁻¹. I–V measurements have been carried out using a Signotron 1160-6N probe station with a heating stage connected to Keithley 4200-SCS semiconductor parameter analyzer.

Device simulation

There are multiple theories for switching mechanisms in resistive switching devices. We have carried out the device simulation using a conductive filament model, which is one of the most popular theories of resistance switching [46, 47] and it has conformed to our experimental data. FEM in COMSOL Multiphysics software has been utilized for the simulation. It has been assumed that the active switching layer in the device constitutes a 'dual conical conductive filament' made of oxygen vacancies in the oxide layer, as proposed by Kim *et al* [3]. It is a simplified geometry of the complex non-linear curvature of the actual filament, which utilizes discontinuous cone geometry, with different slopes for the two sections of the dual-cone. Since the weakest (thinnest) part of the filament will invariably be the one to rupture, such simplified 'dual conical' geometry should yield accurate results, where the thinner section ruptures and the wider section remains intact. Representation of the model can be seen in figure 1. FEM of the electroforming process has also been performed, which further validates the assumed geometry.

GO contains sp³ –C–C– bonds due to the oxidation. Oxygen breaks the regular graphitic sp² –C–C– network and forms out of plane –C–O–C– bonds. Conductivity can be gradually increased by the removal of oxygen. The reduction of GO decreases the number of out of plane bonds, and rGO retains its regular sp² –C–C– bonds with fewer sp³ C–C bonds [48, 49]. The dangling bonds in rGO act as oxygen vacancy sites providing higher conductivity. We have used this idea to develop a model of conductivity, which increases with an increase in the concentration of oxygen vacancies. Hence, the models of electrical and thermal conductivities have been developed as functions of oxygen vacancy concentration. The electrical conductivity of almost zero is taken for GO with no oxygen vacancy concentration, and conductivity similar to that of rGO is taken at high

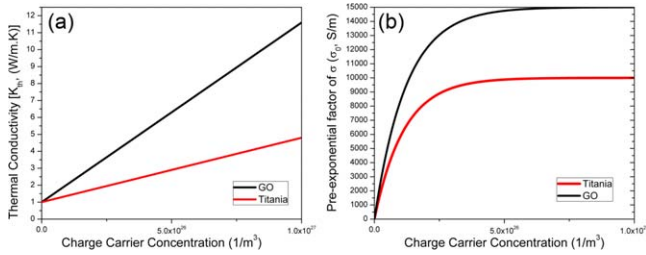


Figure 2. Concentration-dependent models of thermal conductivity (k_{th}) and pre-exponential factor (σ_0) of electric conductivity (σ).

oxygen vacancy concentrations. Such concentration-dependent models have been utilized earlier [41, 42].

In the present work, the I–V measurement probe tip has been used directly as the top electrode. In the I–V measurements, the tungsten probe has been kept in direct contact with the oxide layer. A probe-tip has been previously used as the top electrode to develop ‘top-electrode free’ memristors [50–53]. Hence, the problem of oxygen affinity with the electrode is minimized. Since the electrode is not permanently deposited on the oxide layer, the time of contact between the electrode and the dielectric layer is limited. This limited time of contact of the tungsten probe with the oxides is a reason why interface red-ox reactions have been neglected in the simulation model, with the filamentary process dominating the resistance switching.

Modules and equations used in COMSOL Multiphysics software are the coefficient form of the partial differential equation (PDE), electric currents and heat transfer modules. Additionally, an electrochemistry module for redox reaction has been utilized to account for oxygen vacancy creation during the electroforming process. The coefficient form of the PDE module has been utilized to simulate ‘Fick’s diffusion’ and ‘Mott–Gurney migration’ [54]. At an atomistic level, ionic migration corresponds to ions hopping from one site to another. In the absence of an electric field, this hopping is random. If an electric field is applied, then a net ion flux occurs, which is estimated using Mott–Gurney Law. Since these phenomena are confined to the oxide layer, so is the coefficient form of the PDE module. The electric currents module has been used to control the voltage profiles on the devices, and observe the resultant electric field, current and voltage profiles. Heat transfer in the solids module has been used to apply a temperature, charge conservation, and observe the change in temperature profile due to the current induced, due to various factors. A generation term has been used to account for the dielectric soft breakdown in the oxide layer that leads to the formation/reformation of filaments [41].

The equations involved are as follows.

$$\text{oxygen vacancy transport: } \partial N / \partial t = \nabla \cdot (D \nabla N - \nu N) + G \dots \quad (5)$$

$$\text{current continuity: } \nabla \cdot \sigma \nabla V = 0 \dots \quad (6)$$

$$\text{Joule heating: } \nabla \cdot k_{th} \nabla T = J \cdot E = \sigma |\nabla V|^2 \dots \quad (7)$$

Mott–Gurney electro-migration velocity:

$$\nu = a * f * \exp\left(\frac{E_a}{kT}\right) \sinh\left(\frac{qaE}{2kT}\right) \dots \quad (8)$$

$$\text{generation term: } G = A * \exp\left(-\frac{E_b - q\beta E}{kT}\right) \dots \quad (9)$$

N = concentration of diffusing species; D = diffusion coefficient; J = mass flux, σ = electrical conductivity; a = hopping distance; f = vibration frequency; E_a = activation energy for diffusion; E = electric field; A = pre-exponential factor of generation term; β = simulation mesh size; E_b = energy barrier for ion hopping; $q\beta E$ = barrier reduction due to field application [41, 42].

Equation (5) gives us oxygen vacancy concentration iteratively, which is used to obtain the thermal conductivity and electrical conductivity. These are used to calculate the current for a given voltage, through equations (6) and (7). Oxygen vacancy concentration-dependent models have been used for the parameters involved. The concentration-dependent models of electrical conductivity and thermal conductivity have been provided in figure 2.

For GO, a thermal conductivity plot has been obtained based on [55], and an electrical conductivity plot has been calculated from the sheet resistance and film thickness measured in [56]. For titania, the thermal conductivity values have been estimated from the range obtained from [57–59], and the electrical conductivity pre-exponential factor (σ_0) of the Arrhenius equation has been estimated from [60, 61], with maximum value reaching $10\,000\text{ S m}^{-1}$ [61]. The profile of σ_0 curves has been obtained through cubic interpolation of conductivity data points calculated from known values of current and voltage. The models thus shown in figure 2, have been utilized in the expression of electrical conductivity:

$$\sigma = \sigma_0 \exp\left(\frac{-E_a}{kT}\right).$$

The concentration-dependent thermal conductivity model $k_{th}(N)$ has been used directly.

The mobility of oxygen ions (and hence, oxygen vacancies) has been calculated through the Einstein’s electric mobility equation:

$$\mu = \frac{qD}{kT},$$

where D = diffusion coefficient, k = Boltzmann constant, μ is mobility, q = ionic charge. The diffusion coefficient is obtained through the Arrhenius form of the equation:

$$D = D_0 \exp\left(\frac{-E_a}{kT}\right),$$

D_0 = pre-exponential factor, E_a = activation energy.

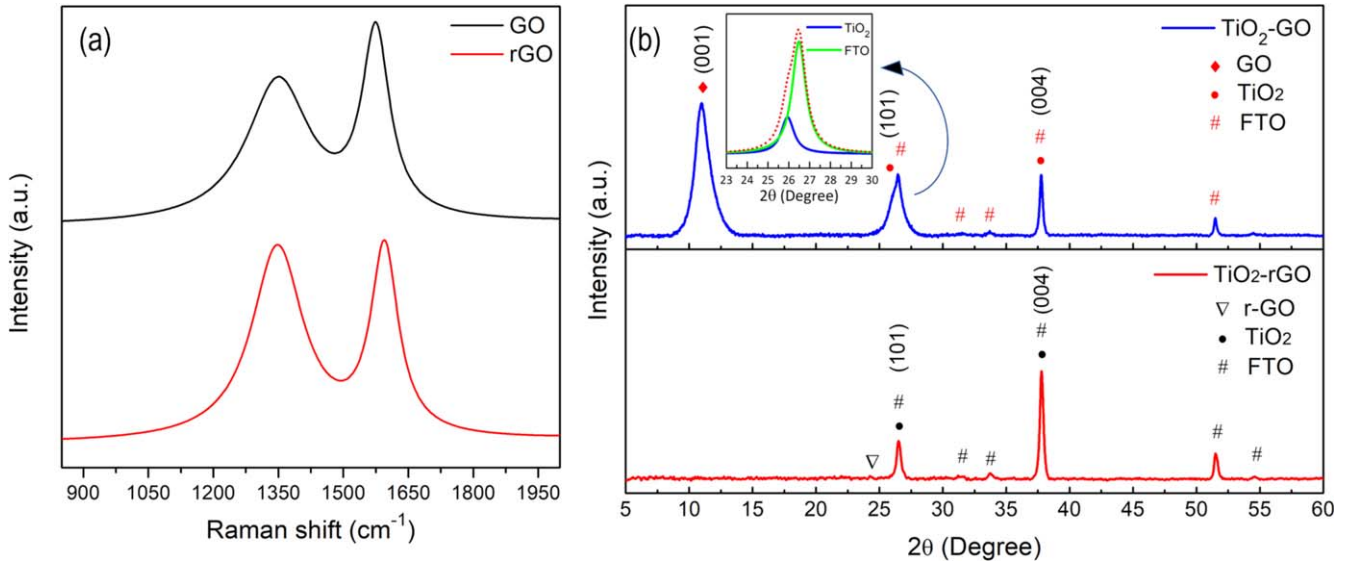


Figure 3. (a) Room temperature Raman spectra of lyophilized GO and rGO, (b) XRD patterns of GO/TiO₂/FTO and rGO/TiO₂/FTO.

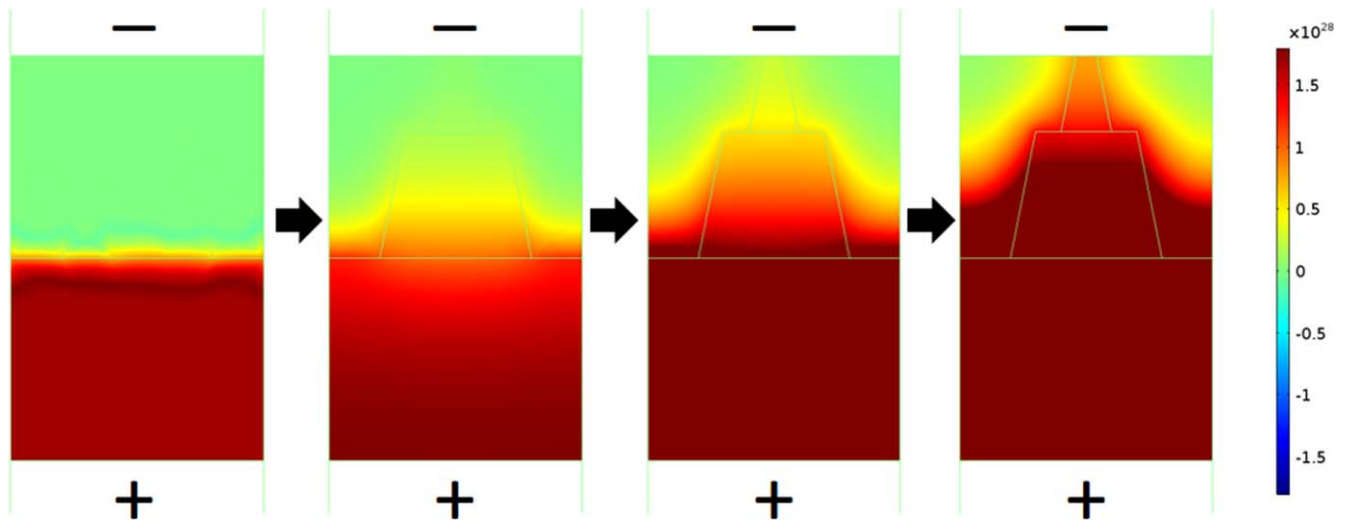


Figure 4. 2D Temporal development of the oxygen vacancy concentration profile, presenting filament formation during electroforming (-10 V) in W/GO/TiO₂/FTO device structure.

Additionally, the forming process involves the electrochemical Butler–Volmer equation [62].

$$i_{BV} = i_o \left(C_R \exp\left(\frac{\alpha_a F \eta}{RT}\right) - C_o \exp\left(\frac{-\alpha_c F \eta}{RT}\right) \right) \dots \quad (10)$$

where, i_{BV} = Butler–Volmer electrode current density; i_o = exchange current density; F = Faraday constant; α_c = dimensionless cathodic charge transfer coefficient; α_a = dimensionless anodic charge transfer coefficient; η = activation over-potential.

The Butler–Volmer equation provides the total current at an electrode, due to electrochemical redox reactions. It equates the net current of cathodic and anodic reaction currents. Equation (10) has been used to obtain the current density of the oxygen vacancies obtained due to the reduction of oxide material near the bottom electrode, aided by the Joule heating process. These vacancies travel towards the top

electrode due to Fick's diffusion, Mott–Gurney electromigration, and Butler–Volmer current, occurring due to the concentration gradient of vacancies and negative forming voltage, respectively. The results are shown in figure 4 for the W/GO/TiO₂/FTO device. The data validates the assumption of a 'dual conical' geometry.

Earlier works have presented a forming process through kinetic Monte Carlo simulations [63], a code of Mott-resistor network [64], etc. However, a simplified FEM model of electroforming has been presented using COMSOL Multiphysics for the first time in the present work.

Results and discussion

The quality of thin films of GO, rGO, and TiO₂ have been investigated by XRD and Raman spectroscopy. For graphite

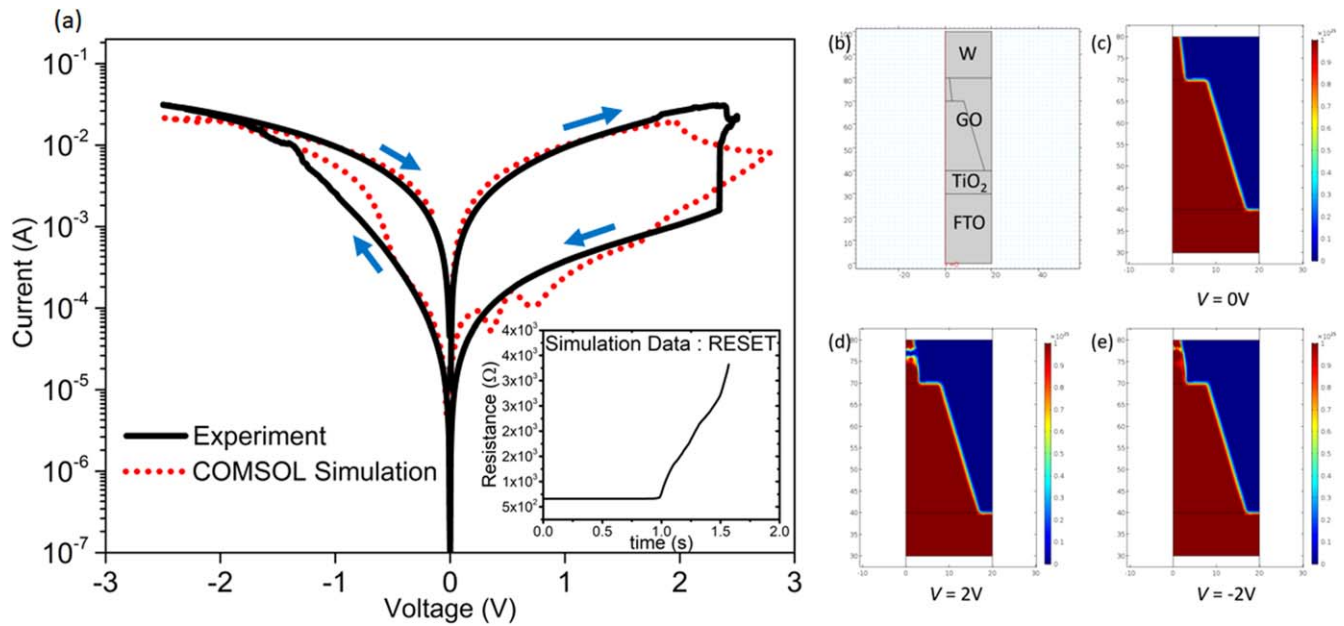


Figure 5. (a) I–V characteristics of simulated and experimental work for W/GO/TiO₂/FTO, (b) simulation axisymmetric geometry, and 2D oxygen vacancy concentration surface plots for W/GO/TiO₂/FTO showing (c) unbroken filament at V = 0, (d) RESET (2 V), (e) SET (–2 V).

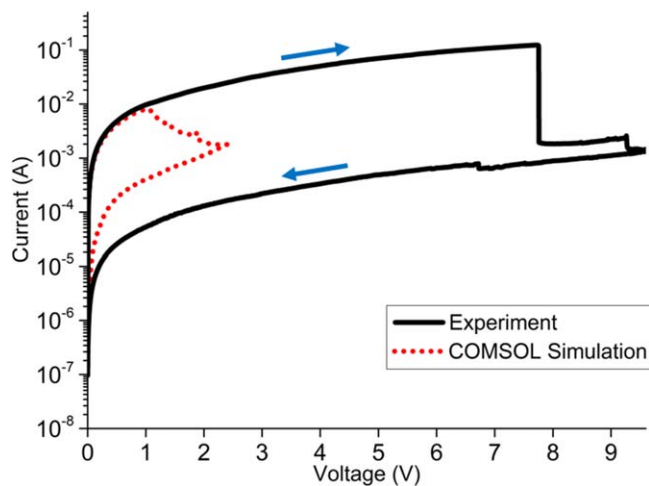


Figure 6. I–V characteristics of simulated and experimental work for W/rGO/TiO₂/FTO, assuming rGO as an active layer.

derivatives, Raman spectroscopy is an inevitable tool. Raman spectra demonstrate the structural changes that happened from pristine graphite to GO. Figure 3(a) depicted the 532 nm Raman spectra of GO and rGO flakes. In GO, the G band appeared at 1595 cm⁻¹. But the G band red shifted to 1584 cm⁻¹ in rGO spectra. G band is the representative of sp² carbon network. It occurred due to the first order phonon scattering (E_{2g} mode) of sp² carbon network. Whereas, D band appeared at 1348 cm⁻¹ of GO Raman spectra, due to the K point phonons of A_{1g} symmetry. In rGO, D band appeared at 1351 cm⁻¹. D band signifies the out of plane vibrations for the defects present in the GO. As mentioned above, reduction of GO decreases the number of out of plane bonds; rGO

retains its regular sp² –C–C– bonds with less number of sp³ C–C bonds.

$$La = (2.4 \cdot 10^{-10}) \lambda^4 (I_D/I_G)^{-1} \dots \quad (11)$$

The increase in the I_D/I_G value, compared to GO in the Raman spectrum of rGO, can be attributed to the increase in the number of sp² domains, and the decrease in the individual crystallite size of the sp² domains, since the crystallite size is inversely proportional to I_D/I_G, since demonstrated in equation (11) [48, 49, 65].

XRD profiles of the thin film layered structures are illustrated in figure 3(b). Both the profiles have exhibited a peak at 2θ = 25.8 and 37.7 degrees [66, 67], which correspond to the (101) and (004) planes, respectively, of the anatase TiO₂ structure. The peak corresponding to the (001) plane of GO has been detected at 10.9 degrees in the TiO₂-GO sample. Whereas, at 24.9 degrees a blunt peak has appeared in the TiO₂-rGO sample, which corresponds to (002) plane of rGO. Observed other XRD peaks have been yielded from the FTO coated glass substrate.

Electroforming has been carried out at a negative bias of –10 V for both the devices. As discussed above, Fick's diffusion, Butler–Volmer current, Mott–Gurney drift and Joule heating have been utilized for FEM of the forming process. Results have been presented in figure 4. The development of oxygen vacancy filament has been presented from left to right. The top electrode has a negative bias of –10 V, while the bottom electrode is grounded. The two layers of materials presented in figure 4 correspond to GO at the top and titania at the bottom, acting as a buffer layer. It can be observed from the final shape of the filament that the dual-conical geometry can be taken as a suitable approximation for the filament

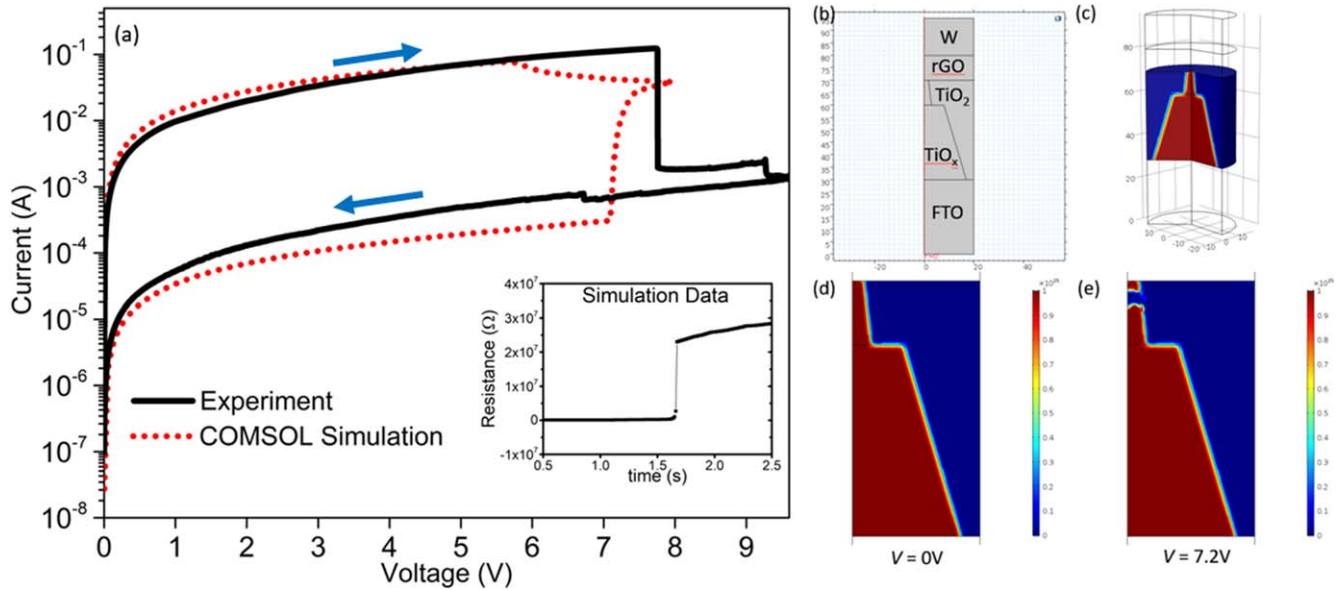


Figure 7. (a) I–V characteristics of simulated and experimental work for W/rGO/TiO₂/FTO, assuming TiO₂ as active layer, (b) proposed geometry of filament formation in TiO₂ layer, (c) 3D representation of filament, (d) oxygen vacancy concentration at $t = 0$, (e) filament breaking after RESET.

geometry. The I–V characteristics have been obtained after the forming process.

To study the switching mechanisms, I–V measurements have been carried out for both the device structures, i.e. W/GO/TiO₂/FTO and W/rGO/TiO₂/FTO. For the W/GO/TiO₂/FTO sample, a voltage sweep of $0 \rightarrow 2.5 \text{ V} \rightarrow -2.5 \text{ V} \rightarrow 0 \text{ V}$ has been done, with W being the top electrode. We obtained the I–V characteristics as shown in figure 5(a). Further, to validate this experimental result, a dual-conical conducting filament model has been adopted through its simulation in COMSOL Multiphysics software. The oxygen vacancies have been simulated to migrate from the TiO₂ layer, which acts as a reservoir of the same, resulting in the formation of a filament in GO layer. In figure 5(a), RESET from low resistance state (LRS) to a high resistance state (HRS) has been obtained under positive bias. As evident from the simulated temporal dependence of resistance presented in the inset of figure 5(a), the gap between the two states is sharp. SET from HRS to LRS has been obtained under negative bias, where the change of state is much more gradual. This is because SET is principally electric field controlled, as opposed to RESET being dependent on two factors—Joule heating and electric field [5]. Figures 5(c)–(e) illustrate the oxygen vacancy concentration surface plots, where GO has been assumed to act as the active filament formation layer.

It is apparent from figure 5(a), for a voltage sweep of $0 \rightarrow 2.5 \text{ V} \rightarrow -2.5 \text{ V} \rightarrow 0 \text{ V}$, we first obtain a RESET around 2 V, where the corresponding simulation of breakage of the filament is presented in figure 5(d). This is followed by SET in the negative voltage regime. Simulation of oxygen vacancy filament formation is shown in figure 5(e). Finally, in figure 5, we obtain a decent overlap of simulation and experimental data in the calculation of the RESET voltage, HRS, and LRS.

Hence, it validates our proposed switching mechanism based on the assumption that in W/GO/TiO₂/FTO, GO acts as the active layer.

In the case of the W/rGO/TiO₂/FTO device, a voltage sweep of $0 \rightarrow 10 \text{ V} \rightarrow 0 \text{ V}$ has been carried out, with W as the top electrode. On performing the I–V characterization experiment, we obtained a sharp RESET at 7.75 V. To validate these results, FEM simulation has been undertaken, assuming rGO as the active layer. However, the simulations have not matched the experimental data, as evident from figure 6.

Figure 6 shows that assuming rGO as the active layer yields theoretical results deviating widely from experimental results. Furthermore, the experimental data of W/rGO/TiO₂/FTO shows that the RESET for the rGO sample occurs at a much higher voltage (7.75 V) than that for the GO sample (2.2 V). If rGO has been the active layer in the rGO-TiO₂ bilayer, then the switching voltage should have been lower than in GO-TiO₂, owing to higher conductivity and charge carrier mobility of rGO. Based on these observations, i.e., mismatch of experimental and simulation data, and higher RESET voltage for the rGO based device, we have proposed that rather than rGO, it is the titania layer which acts as the active layer. This is interesting because a simple reduction of GO layer in the GO-TiO₂ bilayer yields rGO-TiO₂, a device with ~ 3 times higher switching voltage, and an entirely different filament formation layer. To validate this proposition, FEM simulation has been conducted assuming the titania layer to be acting as the switching layer. The model consists of a dual-conical oxygen vacancy conducting filament used for the Magnéli phase of titania, i.e. TiO_x, which forms due to localized Joule heating [68–70]. The conductive rGO layer has been assumed to be part of the top electrode stack (W/rGO). The axisymmetric geometry used for the device is shown in figure 7(c).

The electrical conductivity of the TiO_2 surrounding the TiO_x filament is taken to be much lower, which enables the majority of current to pass through the filament. Hence, on breakage of the filament during RESET, as shown in figure 7, the current drops sharply, putting the device in OFF state. The simulated I–V characteristic of the device is displayed in figure 7(a). The inset figure presents the simulated temporal resistance. Since a single conducting path model has been used in our simulations, we have multiplied the current obtained by a factor of 900 to match with experiments. This indicates that in the rGO– TiO_2 sample, 900 filaments have been forming and breaking simultaneously, similar to the observations by Kim *et al* [3]. By changing our assumption of active layer during simulation, a decent match with the experimental data is obtained. We have obtained a higher switching voltage, sharper switching and higher HRS/LRS ratio, resulting in greater coherency with experimental I–V characteristic, as evident in figure 7(a). This is a testament of the role of rGO as an electrode in rGO/ TiO_2 configuration. So, it can be concluded that GO is a better option for a hybrid RRAM device structure based on TiO_2 .

Conclusion

In conclusion, a bi-layer device configuration has been used to gain insight into the individual roles of GO and rGO in the switching process of RRAM. A 2D dual-conical filament model has been used to numerically solve a set of PDEs, in order to obtain resistance switching in RRAMs to validate our experimental results. FEM has been performed to demonstrate the electroforming process using COMSOL, which has shown the signature of dual-conical filament geometry. A simulation using a oxygen vacancy filament formation and breakage assisted switching model has yielded matching results with experiments. Finally, GO has been found to be the active layer in the GO/ TiO_2 bilayer, while rGO has been observed to act as a mere electrode in the W/rGO/ TiO_2 /FTO configuration. Furthermore, the present work validates the conductive filament model to understand the switching mechanism of a variety of samples, including GO and rGO based RRAMs.

ORCID iDs

Tanmoy Maiti  <https://orcid.org/0000-0003-1581-7614>

References

- [1] Chang T-C, Chang K-C, Tsai T-M, Chu T-J and Sze S M 2016 Resistance random access memory *Mater. Today* **19** 254–64
- [2] Puglisi F M, Pavan P, Padovani A and Larcher L 2014 A study on HfO_2 RRAM in HRS based on I–V and RTN analysis *Solid. State. Electron.* **102** 69–75
- [3] Kim K M, Park T H and Hwang C S 2015 Dual conical conducting filament model in resistance switching TiO_2 thin films *Sci. Rep.* **5** 7844
- [4] Hua-Yu W, Jian Z, Qi-Long Z, Hui Y and Luo J K 2014 Electroforming-free and highly uniform Al_2O_3 resistive random access memory by ALD-based *in situ* hydrogen plasma treatment *Chin. Phys. Lett.* **31** 057305
- [5] Asapu S and Maiti T 2017 Multifilamentary conduction modeling in transition metal oxide-based RRAM *IEEE Trans. Electron Devices* **64** 3145–50
- [6] Qi J, Olmedo M, Ren J, Zhan N, Zhao J, Zheng J-G and Liu J 2012 Resistive switching in single epitaxial ZnO nanoislands *ACS Nano* **6** 1051–8
- [7] Koza J A, He Z, Miller A S and Switzer J A 2011 Resistance switching in electrodeposited VO_2 thin films *Chem. Mater.* **23** 4105–8
- [8] Hwan K C, Yoonho A and Yeog S J 2015 Sr TiO_3 -based resistive switching memory device with graphene nanoribbon electrodes *J. Am. Ceram. Soc.* **99** 9–11
- [9] Bogusz A, Bürger D, Skorupa I, Schmidt O G and Schmidt H 2016 Bipolar resistive switching in $\text{YMnO}_3/\text{Nb:SrTiO}_3$ pn-heterojunctions *Nanotechnology* **27** 455201
- [10] Pradel A, Frolet N, Ramonda M, Piarristeguy A and Ribes M 2011 Bipolar resistance switching in chalcogenide materials *Phys. Status Solidi* **208** 2303–8
- [11] Lee M-J *et al* 2011 A fast, high-endurance and scalable non-volatile memory device made from asymmetric $\text{Ta}_2\text{O}_{5-x}/\text{TaO}_{2-x}$ bilayer structures *Nat. Mater.* **10** 625
- [12] Banerjee W, Rahaman S Z, Prakash A and Maikap S 2011 High- κ $\text{Al}_2\text{O}_3/\text{WO}_x$ bilayer dielectrics for low-power resistive switching memory applications *Jpn. J. Appl. Phys.* **50** 10PH01
- [13] Lee J, Bourim E M, Lee W, Park J, Jo M, Jung S, Shin J and Hwang H 2010 Effect of $\text{ZrO}_x/\text{HfO}_x$ bilayer structure on switching uniformity and reliability in nonvolatile memory applications *Appl. Phys. Lett.* **97** 172105
- [14] Song Y L, Liu Y, Wang Y L, Wang M, Tian X P, Yang L M and Lin Y Y 2011 Low reset current in stacked AlO_x/WO_x resistive switching memory *IEEE Electron Device Lett.* **32** 1439–41
- [15] Santini C A, Sebastian A, Marchiori C, Jonnalagadda V P, Dellmann L, Koelmans W W, Rossell M D, Rossel C P and Eleftheriou E 2015 Oxygenated amorphous carbon for resistive memory applications *Nat. Commun.* **6** 8600
- [16] Sebastian A, Pauza A, Rossel C, Shelby R M, Rodríguez A F, Pozidis H and Eleftheriou E 2011 Resistance switching at the nanometre scale in amorphous carbon *New J. Phys.* **13** 13020
- [17] Jeong H Y *et al* 2010 Graphene oxide thin films for flexible nonvolatile memory applications *Nano Lett.* **10** 4381–6
- [18] Hui F, Grustan-Gutierrez E, Long S, Liu Q, Ott A K, Ferrari A C and Lanza M 2017 Graphene and related materials for resistive random access memories *Adv. Electron. Mater.* **3** 1600195 –n/a
- [19] Nagareddy V K, Barnes M D, Zipoli F, Lai K T, Alexeev A M, Craciun M F and Wright C D 2017 Multilevel ultrafast flexible nanoscale nonvolatile hybrid graphene oxide–titanium oxide memories *ACS Nano* **11** 3010–21
- [20] Ji Y, Lee S-A, Cha A-N, Goh M, Bae S, Lee S, Son D I and Kim T-W 2015 Resistive switching characteristics of ZnO –graphene quantum dots and their use as an active component of an organic memory cell with one diode–one resistor architecture *Org. Electron.* **18** 77–83
- [21] Kim I, Siddik M, Shin J, Biju K P, Jung S and Hwang H 2011 Low temperature solution-processed graphene oxide/ $\text{Pr}_{0.7}\text{Ca}_{0.3}\text{MnO}_3$ based resistive-memory device *Appl. Phys. Lett.* **99** 42101
- [22] Kreupl F 2014 Carbon memory assessment *White Paper for the ITRS Meeting on Emerging Research Devices (ERD) (Albuquerque, New Mexico, August 25–26)*
- [23] Thakre A and Kumar A 2017 Bipolar resistive switching in PVDF and graphene oxide hetero-structure thin films *J. Alloys Compd.* **722** 579–84

- [24] Chao H, Yuan F Y, Wu H, Deng N, Yu Z Z and Wei R 2015 Graphene oxide and TiO₂ nano-particle composite based nonvolatile memory *2015 15th Non-Volatile Memory Technology Symp. (NVMTS)* pp 1–4
- [25] Yi M, Cao Y, Ling H, Du Z, Wang L, Yang T, Fan Q, Xie L and Huang W 2014 Temperature dependence of resistive switching behaviors in resistive random access memory based on graphene oxide film *Nanotechnology* **25** 185202
- [26] Wright C D CareRAMM public summary: http://emps.exeter.ac.uk/media/universityofexeter/emps/careramm/D4.4_Public_summary_of_project_results_from_the_third_year_of_the_project.pdf (Accessed: August 2018)
- [27] Hong S K, Kim J E, Kim S O, Choi S Y and Cho B J 2010 Flexible resistive switching memory device based on graphene oxide *IEEE Electron Device Lett.* **31** 1005–7
- [28] Liu S, Lu N, Zhao X, Xu H, Banerjee W, Lv H, Long S, Li Q, Liu Q and Liu M 2016 Eliminating negative-SET behavior by suppressing nanofilament overgrowth in cation-based memory *Adv. Mater.* **28** 10623–9
- [29] Zhang B, Liu G, Chen Y, Zeng L-J, Zhu C-X, Neoh K-G, Wang C and Kang E-T 2011 Conjugated polymer-grafted reduced graphene oxide for nonvolatile rewritable memory *Chem.—A Eur. J.* **17** 13646–52
- [30] Chakrabarti B, Roy T and Vogel E M 2014 Nonlinear switching with ultralow reset power in graphene-insulator-graphene forming-free resistive memories *IEEE Electron Device Lett.* **35** 750–2
- [31] Lee S, Sohn J, Jiang Z, Chen H-Y and Philip Wong H-S 2015 Metal oxide-resistive memory using graphene-edge electrodes *Nat. Commun.* **6** 8407
- [32] Jiang H, Han L, Lin P, Wang Z, Jang M H, Wu Q, Barnell M, Yang J J, Xin H L and Xia Q 2016 Sub-10 nm Ta channel responsible for superior performance of a HfO₂ memristor *Sci. Rep.* **6** 28525
- [33] Lee H Y *et al* 2010 Evidence and solution of over-RESET problem for HfO_x based resistive memory with sub-ns switching speed and high endurance *2010 Int. Electron Devices Meeting* pp 1–19
- [34] Zhou J, Cai F, Wang Q, Chen B, Gaba S and Lu W D 2016 Very low-programming-current RRAM with self-rectifying characteristics *IEEE Electron Device Lett.* **37** 404–7
- [35] Wei Z *et al* 2008 Highly reliable TaO_x ReRAM and direct evidence of redox reaction mechanism *2008 IEEE Int. Electron Devices Meeting* pp 1–4
- [36] Cao X, Li X, Gao X, Yu W, Liu X, Zhang Y, Chen L and Cheng X 2009 Forming-free colossal resistive switching effect in rare-earth-oxide Gd₂O₃ films for memristor applications *J. Appl. Phys.* **106** 73723
- [37] Chou C-T, Hudec B, Hsu C-W, Lai W-L, Chang C-C and Hou T-H 2015 Crossbar array of selector-less TaO_x/TiO₂ bilayer RRAM *Microelectron. Reliab.* **55** 2220–3
- [38] Xiao N *et al* 2017 Resistive random access memory cells with a bilayer TiO₂/SiO_x insulating stack for simultaneous filamentary and distributed resistive switching *Adv. Funct. Mater.* **27** 1700384
- [39] Banerjee W, Xu X, Lv H, Liu Q, Long S and Liu M 2017 Variability improvement of TiO_x/Al₂O₃ bilayer nonvolatile resistive switching devices by interfacial band engineering with an ultrathin Al₂O₃ dielectric material *ACS Omega* **2** 6888–95
- [40] Ye C, Deng T, Zhang J, Shen L, He P, Wei W and Wang H 2016 Enhanced resistive switching performance for bilayer HfO₂/TiO₂ resistive random access memory *Semicond. Sci. Technol.* **31** 105005
- [41] Kim S, Kim S-J, Kim K M, Lee S R, Chang M, Cho E, Kim Y-B, Kim C J, In Chung U and Yoo I-K 2013 Physical electro-thermal model of resistive switching in bi-layered resistance-change memory *Sci. Rep.* **3** 1680
- [42] Kim S, Choi S and Lu W 2014 Comprehensive physical model of dynamic resistive switching in an oxide memristor *ACS Nano* **8** 2369–76
- [43] Hummers W S and Offeman R E 1958 Preparation of graphitic oxide *J. Am. Chem. Soc.* **80** 1339
- [44] Vivo P *et al* 2017 Influence of TiO₂ compact layer precursor on the performance of perovskite solar cells *Org. Electron.* **41** 287–93
- [45] Dey P, Khorwal V, Sen P, Biswas K and Maiti T 2018 Spectral studies of lead-free organic-inorganic hybrid solid-state perovskites CH₃NH₃Bi₂/3I₃ and CH₃NH₃Pb₁/2Bi₁/3I₃: potential photo absorbers *ChemistrySelect.* **3** 794–800
- [46] Gibbons J F and Beadle W E 1964 Switching properties of thin NiO films *Solid. State. Electron.* **7** 785–90
- [47] Ielmini D 2011 Modeling the universal set/reset characteristics of bipolar RRAM by field- and temperature-driven filament growth *IEEE Trans. Electron Devices* **58** 4309–17
- [48] Ferrari A C and Robertson J 2000 Interpretation of Raman spectra of disordered and amorphous carbon *Phys. Rev. B* **61** 14095–107
- [49] Stankovich S, Dikin D A, Piner R D, Kohlhaas K A, Kleinhammes A, Jia Y, Wu Y, Nguyen S T and Ruoff R S 2007 Synthesis of graphene-based nanosheets via chemical reduction of exfoliated graphite oxide *Carbon NY.* **45** 1558–65
- [50] Hsu C, Chuang P and Chen Y 2017 Resistive switching characteristic of low-temperature top-electrode-free tin-oxide memristor *IEEE Trans. Electron Devices* **64** 3951–4
- [51] Lanza M 2014 A review on resistive switching in high-k dielectrics: a nanoscale point of view using conductive atomic force microscope *Mater.* **7** 2155–82
- [52] Gao X, Zhang X, Wan C, Wang J, Tan X and Zeng D 2012 Temperature-dependent resistive switching of amorphous carbon/silicon heterojunctions *Diam. Relat. Mater.* **22** 37–41
- [53] Fisichella G, Greco G, Roccaforte F and Giannazzo F 2014 Current transport in graphene/AlGaIn/GaN vertical heterostructures probed at nanoscale *Nanoscale* **6** 8671–80
- [54] Mott N F and Gurney R W 1948 *Electronic Processes in Ionic Crystals* (Oxford: Clarendon)
- [55] Mu X, Wu X, Zhang T, Go D B and Luo T 2014 Thermal transport in graphene oxide—from ballistic extreme to amorphous limit *Sci. Rep.* **4** 3909
- [56] Eda G, Fanchini G and Chhowalla M 2008 Large-area ultrathin films of reduced graphene oxide as a transparent and flexible electronic material *Nat. Nanotechnol.* **3** 270
- [57] Maekawa T, Kurosaki K, Tanaka T and Yamanaka S 2008 Thermal conductivity of titanium dioxide films grown by metal–organic chemical vapor deposition *Surf. Coatings Technol.* **202** 3067–71
- [58] Arif A F, Balgis R, Ogi T, Iskandar F, Kinoshita A, Nakamura K and Okuyama K 2017 Highly conductive nano-sized Magnéli phases titanium oxide (TiO_x) *Sci. Rep.* **7** 3646
- [59] Pandey S J, Joshi G, Wang S, Curtarolo S and Gaume R M 2016 Modeling the thermoelectric properties of Ti₅O₉ Magnéli phase ceramics *J. Electron. Mater.* **45** 5526–32
- [60] Bartholomew R F and Frankl D R 1969 Electrical properties of some titanium oxides *Phys. Rev.* **187** 828–33
- [61] Adamaki V, Clemens F, Ragulis P, Pennock S R, Taylor J and Bowen C R 2014 Manufacturing and characterization of Magnéli phase conductive fibres *J. Mater. Chem. A* **2** 8328–33
- [62] Bockris J O, Reddy A K N and Gamboa-Aldeco M 2000 *Modern Electrochemistry: Fundamentals of Electrodeics* (Kluwer Academic/Plenum Publishers)
- [63] Pan F, Yin S and Subramanian V 2011 A comprehensive simulation study on metal conducting filament formation in

- resistive switching memories *2011 3rd IEEE Int. Memory Workshop (IMW)* pp 1–4
- [64] Stoliar P, Rozenberg M, Janod E, Corraze B, Tranchant J and Cario L 2014 Nonthermal and purely electronic resistive switching in a Mott memory *Phys. Rev. B* **90** 45146
- [65] Tuinstra F and Koenig J L 1970 Raman spectrum of graphite *J. Chem. Phys.* **53** 1126–30
- [66] Wang W-K, Chen J-J, Zhang X, Huang Y-X, Li W-W and Yu H-Q 2016 Self-induced synthesis of phase-junction TiO₂ with a tailored rutile to anatase ratio below phase transition temperature *Sci. Rep.* **6** 20491
- [67] Thamaphat K, Limsuwan P and Ngotawornchai B 2008 Phase characterization of TiO₂ powder by XRD and TEM *Nat. Sci.* **42** 357–61
- [68] Strachan J P, Pickett M D, Yang J J, Aloni S, David Kilcoyne A L, Medeiros-Ribeiro G and Stanley Williams R 2010 Direct identification of the conducting channels in a functioning memristive device *Adv. Mater.* **22** 3573–7
- [69] Carta D, Hitchcock A P, Guttmann P, Regoutz A, Khiat A, Serb A, Gupta I and Prodrumakis T 2016 Spatially resolved TiO_x phases in switched RRAM devices using soft x-ray spectromicroscopy *Sci. Rep.* **6** 21525
- [70] Strachan J P, Yang J J, Münstermann R, Scholl A, Medeiros-Ribeiro G, Stewart D R and Williams R S 2009 Structural and chemical characterization of TiO₂ memristive devices by spatially-resolved NEXAFS *Nanotechnology* **20** 485701